RSC
Applied Polymers

ROYAL SOCIETY
OF CHEMISTRY

PAPER
Katharina Ehrmann *et al.*
Thermoplastic-like mechanical performance of
heterogeneous photopolymers for additive manufacturing
with tailored hyperbranched rubbers

Thermoplastic-like mechanical performance of heterogeneous photopolymers for additive manufacturing with tailored hyperbranched rubbers

Vojtěch Musil, [ID] [a] Dominik Laa, [ID] [b] Mojtaba Ahmadi, [ID] [b] Jürgen Stampfl, [ID] [b] Robert Liska, [ID] [c] Jan Merna [ID] [a] and Katharina Ehrmann [ID] *[c]

Conventional photopolymers used in light-based additive manufacturing are typically brittle materials with thermoset characteristics. Here we introduce a one-step synthesis of hyperbranched polyethylene rubbers functionalized with pendant methacrylic groups and their application as tougheners of a model brittle photopolymer based on non-volatile styrene and maleimide derivatives. The rubber tougheners can be tailored to tune their compatibility with the matrix, influencing the morphology and the thermo-mechanical properties of the final printed resins. The resulting polymer structures were analysed by atomic force microscopy, revealing various degrees of phase separation related to the rubber molar mass and methacrylate functionalization. Further, the analysis of the prepared toughened materials revealed the ability of functionalized hyperbranched polyethylene rubbers to improve the mechanical properties significantly (doubled stress at break and improvement of strain at break by a factor of 10^3 compared to the matrix), while glass transition temperatures around 100 °C could be maintained. Notably, even tensile behaviour mimicking typical thermoplastic yield strain comparable to ABS was observed in one of the prepared materials. This monomer/rubber system appeared to be the most promising and was therefore selected for in-depth analysis of the curing process using photo-rheology and photo-DSC. Finally, this material was used for hot lithography and several highly detailed objects were prepared, demonstrating the good printability of this toughened material.

Introduction

In recent years, additive manufacturing technologies have been on the rise due to their versatility, fast adaptability to ever-changing market trends, and the ability to fabricate products with complex structures, which are almost impossible to make using conventional manufacturing methods.[1–3] In particular, the field of vat photopolymerization is advancing rapidly, which features numerous advantages over extrusion-based additive manufacturing: higher print resolution,[4] better inter-layer adhesion,[5] faster print speeds due to simultaneous curing of entire layers by digital light processing (DLP),[6] printability of more complex geometries and overall lower waste production from support structures.[7] Currently, one of the main limitations of vat photopolymerization is the insufficient thermomechanical properties of printed photopolymers: very stiff photopolymer networks with high glass transition temperatures (T_gs) typically fracture brittle, without any reversible (elastic) or irreversible (plastic) deformation of the specimen prior to failure. The most commonly used highly reactive acrylate monomers form inhomogeneous, highly crosslinked polymer networks resulting in the described very hard and stiff but brittle polymers.[8,9]

However, such deformation behaviour would be particularly important during application as a warning sign for imminent material failure. Therefore, alternative monomer systems and strategies for improving photopolymers' strain at break while maintaining high stiffness and onsets of their T_gs, and ideally introducing yielding behaviour, are investigated. Alternative polymerization methods (*e.g.* dual-cure networks,[9] interpenetrating networks,[10] thiol–ene chemistry[11]) can be used but especially rubber toughening methods inspired by thermoplastic toughening seem like a straightforward alternative for this purpose.[12]

The potency of rubber toughening has been demonstrated countless times in a variety of polymeric materials,[13–15] includ-

aDepartment of Polymers, University of Chemistry and Technology, Prague, Technická 5, 166 28 Prague 6, Czech Republic
bInstitute of Materials Science and Technology, Technische Universität Wien, Vienna, Austria
cInstitute of Applied Synthetic Chemistry, Technische Universität Wien, Vienna, Austria. E-mail: katharina.ehrmann@tuwien.ac.at

ing famous engineering plastics such as acrylonitrile-buta-diene-styrene (ABS).[16–18] In the area of photopolymers for 3D printing, however, rubber toughening faces several challenges for successful implementation due to strict requirements of the formulation. First and foremost, photocurable resins for vat photopolymerization are limited by their viscosity. If the viscosity is too high, the resin cannot flow sufficiently to recoat the printing interface and therefore printing speed and quality are impaired.[19,20] Secondly, the rubber must be miscible with the photopolymer matrix components to create homogeneous formulations in the vat. This severely limits the molecular weight of utilized rubbers as well as the amount of rubber, which can be incorporated into the matrix. Thirdly, homogenous distribution of rubber phases throughout the material must be ensured for superior thermomechanical performance with high glass transition temperatures and yet stiff and yielding tensile behaviour compared to the unmodified photopolymer, which is particularly challenging when rubbers are incorporated without covalent bonding to the photopolymer matrix.[21]

Despite these challenges in incorporating rubbers in photopolymeric formulations, the vat photopolymerization community has demonstrated several approaches for rubber toughening. The unsatisfactory strain at break of brittle photopolymers could for example be improved through addition of core–shell particles or reactive rubbers.[22] Lower molar mass reactive rubbers are particularly compatible with photopolymeric matrices and can bind to the matrix covalently, ensuring their homogeneous distribution. However, the addition of low molar mass rubbers typically disrupts the rigid matrix network ultimately leading to a decreased thermal resistance and glass transition temperature.[23] Core–shell particles often require labour intensive synthesis and therefore tend to be quite costly.[24] While common diene-based elastomers are cheap and have been shown to improve the strain at break effectively, they typically also soften the material, *i.e.* lower the initial high stress response. Additionally, these elastomers are limited by their reactivity and ability to bind to the matrix covalently.[21] This challenge can be addressed with post-polymerization procedures that increase their reactivity. However, this usually includes a very difficult multistep synthesis, which radically increases their price.[25] Additionally, diene-based elastomers tend to suffer from oxidative degradation, which limits the longevity of the toughened material.[26]

We propose to overcome these obstacles by using functionalized hyperbranched polyolefins as macromonomers. Although hyperbranched polymers are historically viewed as costly and difficult to synthesize,[27] the discovery of nickel- and palladium-based α-diimine catalysts has provided an innovative approach for the facile one-pot synthesis of functional polyolefins with various molecular architectures.[28] Compared to conventional Ziegler polyinsertion catalysts, Ni- and Pd-based α-diimine catalysts offer several advantages. Their precise topology control *via* chain walking isomerisation allows the synthesis of a broad spectrum of polyolefin materials ranging from linear semi-crystalline thermoplastics to liquid amorphous hyperbranched elastomers.[29–31] Additionally, Pd-diimine catalysts exhibit superior tolerance towards polar groups, enabling direct copolymerization with polar monomers and thus pendant-group functionalization of the polyolefins, which enables their covalent incorporation into the photopolymeric matrix.[32,33] Despite numerous published attempts to copolymerize ethene with dienes or di(meth)acrylates, stable chelate formation, catalyst poisoning, cyclization and *in situ* crosslinking complicate efficient polyethylene functionalization with reactive double bonds.[34–38] Although functionalization with double bonds can be achieved by post-polymerization modifications, it complicates the process and increases manufacturing costs.[39]

Herein, we present a synthetic approach for the preparation of hyperbranched polyethylene rubbers functionalized with pendant methacrylic end groups (Scheme 1). Hyperbranched molecule architectures are highly branched, non-crosslinked dendritic bottlebrush molecules. Since they exhibit many end groups, partial functionalization of the end groups of such molecules already guarantees superior function of the resulting molecules as crosslinkers. Such functionalized hyperbranched polyethylene rubbers can thus act as macro-
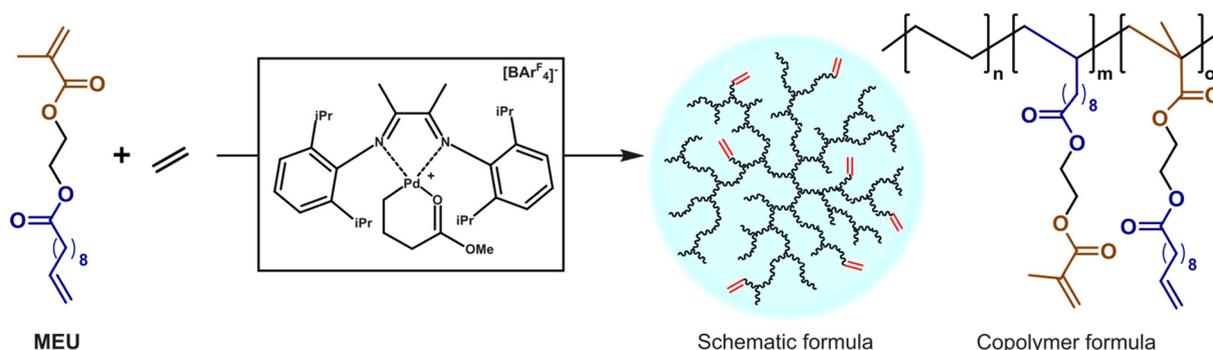
Scheme 1 Copolymerization of ethene with 2-(methacryloyloxy)ethyl undec-10-enoate (**MEU**) by a chain walking Pd-complex (**Pd**) into hyperbranched, methacrylate-containing polyethylene macromonomer. The resulting copolymer formula of the macromonomer is displayed on the right-hand side.

monomers with crosslinking ability, which ascertains homogeneous distribution of these hyperbranched polyethylene rubber molecules throughout the polymer matrix *via* covalent incorporation in the network. To prepare these hyperbranched macromonomers, the hyperbranched rubbers are functionalized with a tailored comonomer during their synthesis, which terminates already formed branches, thereby forming functional end groups. Herein, functionalized hyperbranched rubbers with various molar masses and methacrylate contents have been synthesized by utilizing Pd-based α-diimine catalysts. They have been tested as macromonomers for rubber toughening of brittle photopolymers in 3D printing. Hot Lithography was employed as printing process to manage the macromonomers' viscosity and miscibility. This approach introduces a highly tuneable monomer class, which ticks several boxes for their incorporation in 3D printable photopolymer formulations: they exhibit comparably low viscosities despite high molecular weights and their end group functionalization facilitates polarity tuning for convenient copolymerization with standard monomers for photopolymerization as well as covalent incorporation of these rubbery molecules into the polymer network, which allows for homogeneous distribution of the rubber phase throughout the polymer matrix and highly controlled microstructuring of the photopolymer.

Results and discussion

Preparation of methacrylate-functionalized hyperbranched polyethylene rubbers

Hyperbranched architectures can be achieved during the synthesis of polyethylene utilizing chain-walking metal catalysts. However, such catalysts are typically highly sensitive to polar functional groups, which coordinate to the metal center and thereby deactivate ("poison") the catalyst. To introduce reactive methacrylate end groups during the synthesis of hyperbranched polyethylene nonetheless, the previously introduced Pd diimine complex (**Pd**, Scheme 1) is employed as catalyst, which exhibits superior functional group tolerance.[40] For the catalysed copolymerization with ethene, our search for a suitable comonomer to introduce the functional end groups identified ethylene glycol diester 2-(methacryloyloxy)ethyl

undec-10-enoate (**MEU**) as suitable candidate to give a non-crosslinked hyperbranched macromonomer with acceptable molar mass (4.3–31.8 kg mol^{-1}, Scheme 1) and good yield. **MEU** contains a sterically accessible double bond prone to catalyst insertions in the 10-undecenoyl group and a long linker separating it from the sterically hindered methacrylic group that is unfavourable for catalyst insertion. This structure mitigates both *in situ* crosslinking and a severe decrease in the catalyst activity caused by chain walking and subsequent palladium poisoning typically observed with dienes.[36,37]

Three different hyperbranched polyethylene rubbers were prepared as macromonomers in this way, each varying in molar mass and **MEU** content (Table 1). In the following, all macromonomers will be referred to as *x***PE**, whereby *x* can be 0, 1 or 2, and signifies increasing amounts of end groups introduced *via* **MEU** (x_{meth} = 0, 0.7, and 2.5 mol%, respectively). **0PE** samples thus include unreactive, apolar rubber in the photopolymer matrix, while **1PE** and **2PE** utilize functionalized hyperbranched rubbers of different degrees of functionalization and different molecular weights, which are included into the matrix covalently. While the reaction yield did not decrease severely even at a high **MEU** comonomer concentration of 0.4 mol L^{-1}, the macromonomer molar mass plummeted from 119 kg mol^{-1} (non-functionalized hyperbranched polyethylene reference, **0PE**) to 4.3 kg mol^{-1} (hyperbranched polyethylene containing 2.5 mol% methacrylate, **2PE**). Although typical industrial rubber toughening agents are high molecular weight rubbers, low molecular weight liquid rubbers were proven to be a suitable choice for thermosets since they also effectively contribute to microphase separation.[9,41] In fact, the low molar mass contributes to the rubber compatibility with the matrix, which influences maximum rubber content and rubber domain size in the microstructure.

In addition to **0PE**, a second, more polar reference macromonomer was synthesized, which contains unreactive ethyl ester end groups (**EPE**), to investigate the effect of the reactive bonds on the microphase separation for rubbers with similar molecular weight and polarity. **0PE** and **EPE** cannot react with the matrix monomer system and therefore do not contribute to the rubber/matrix compatibility by binding to the matrix covalently. At the same time, the polar end groups of **EPE** allow homogeneous mixing with the matrix components, which was

Table 1 Macromonomers prepared as copolymers of ethene and **MEU** or ethyl undecenoate (**1PE**, **2PE**, catalyzed by **Pd**[a]) and their properties compared to pure hyperbranched polyethylene (**0PE**) and its more polar unreactive analogue containing ethyl ester endgroups (**EPE**): methacrylic ester group content determined by ^{1}H-NMR (x_{meth}), 10-undecenoic ester group content determined by ^{1}H-NMR (x_{unde}), degree of branching in branches per 1000 carbon atoms determined by ^{1}H-NMR (*B*), number average molar mass determined by SEC (M_n)

Rubber	[MEU]/mol L^{-1}	*V*/mL	Yield/g	x_{meth}/mol%	x_{unde}/mol%	M_n/kg mol^{-1}	M_w/M_n/—	*B*/10^{-3} C
0PE	—	30	14.5	—	—	119.0	2.1	97
EPE	—[b]	100	8.4	—[b]	—[b]	30.4	1.6	98
1PE	0.1	100	11.3	0.7	0.1	31.8	3.0	94
2PE	0.4	100	5.7	2.5	0.3	4.3	2.0	89

[a] Conditions: solvent dichloromethane, 24 h, 35 °C, 2.5 atm ethene (absolute pressure), 10 μmol **Pd**. [b] Performed with 0.15 mol L^{-1} ethyl undecenoate as a comonomer instead of **MEU** at 2 atm ethene (absolute pressure) leading to 3.2 mol% incorporation of ethyl ester end groups.

not possible with **0PE**. To facilitate comparisons based on the covalent rubber incorporation *vs.* incorporation of rubbers as filler, the molar mass of the **EPE** reference (30.4 kg mol^{-1}) is tailored to be comparable to the molar mass of the first functionalized rubber **1PE** (31.8 kg mol^{-1}).

Toughening of styrene-maleimide resin

Based on a previous ABS-mimicking photopolymer approach, we found styrene-maleimide copolymers to be a suitable photopolymerizable matrix for rubber toughening.[21] However, in our previous approach, microstructured domains similar to ABS could not be obtained due to the incorporation of the butadiene rubber with its double bonds along the main chain, which deteriorated the ability for photopolymerization-induced phase separation. Based on these findings, we utilized the optimal maleimide-styrene matrix in the approach herein.

Nine formulations based on non-volatile maleimide and styrene derivatives in a molar ratio of 1 : 2 were prepared (Scheme 2 and Table 2). The prepared hyperbranched rubbers were added at varying loadings of 10, 15 or 20 wt%. Thereby, the photocuring temperature of 80 °C enabled sufficient miscibility of the rubber macromonomers with the matrix monomers. The non-functionalized hyperbranched rubber **0PE** was found to hinder the photo-solidification process due to the lack of reactive double bonds crucial for the formation of a crosslinked network. Adding just 10 wt% of **0PE** already deteriorated the resin cohesion to such an extent that the solidified polymer disintegrated with very little force applied, making it impossible to evaluate its thermomechanical properties. Higher **0PE** loading worsened the resin curing and final properties even more, resulting in a sticky powder instead of a solid polymer. On the other hand, the functionalized hyperbranched rubbers **1PE** and **2PE** accelerated the curing and provided solid polymers.

The prepared materials were analysed using dynamic mechanical thermal analysis (DMTA, Table 2 and Fig. 1) from −100 °C up to the temperatures triggering their softening-induced measurement failure. While all samples exhibited slightly lower T_g onsets compared to the pure matrix, the ultimate glass transition temperature increased in samples toughened by **1PE** rubber up to 147 °C. This can be attributed to both increased crosslinking density and hindered matrix chain mobility compared to non-toughened samples. On the con-

Table 2 Prepared formulations and their thermomechanical properties: storage modulus at 25 °C ($G'_{25°C}$), and glass transition temperature (T_g)

| Formulation | Rubber | | $G'_{25°C}$ /GPa | T_g/°C |
	Type	Content/wt%		
Matrix	—	—	0.96	97
0PE10	**0PE**	10	—[a]	—[a]
EPE10	**EPE**	10	—[a]	—[a]
1PE10	**1PE**	10	0.61	117
1PE15	**1PE**	15	0.34	122
1PE20	**1PE**	20	0.36	147
2PE10	**2PE**	10	0.49	98
2PE15	**2PE**	15	0.44	98
2PE20	**2PE**	20	0.41	97

[a] Too brittle for testing.

trary, the tested specimens containing the low molecular weight rubber **2PE** exhibit a T_g comparable to the non-toughened matrix (97–98 °C). This can be easily explained as the small **2PE** molecules are not expected to significantly influence the two parameters most relevant to a material's T_g, matrix chain mobility and the materials' crosslinking density.

The prepared materials were further analysed in tensile tests and the functionalized hyperbranched rubbers **1PE** and **2PE** were both found to improve the resulting mechanical properties significantly (Table 3 and Fig. 2). While 10 and 15 wt% rubber loading lead to an increase in both, the maximum tensile strength (σ) and the elongation at break (ε) compared to the pure matrix, the tensile curves were still characteristic for crosslinked thermosets and failed to mimic the thermomechanical behaviour of thermoplastic materials.

Interestingly, cured formulations **1PE20** and **2PE20** had substantially different tensile properties compared to all other formulations. At this highest rubber content, the lower molecular weight rubber with more reactive functional end groups **2PE** outperforms **1PE**: **1PE20** behaved similarly to our previously reported poly(buta-1,3-diene) toughened networks.[21] After a steep rise in tensile stress at still low elongation, the rubbery behaviour of the material starts to dominate and achieves 51.3% elongation at break. This tensile testing curve shape is typical for polymers, which undergo significant softening due to the incorporation of rubber. For **2PE20**, however, typical thermoplastic thermomechanical behaviour with a yield point at 12.3 ± 0.7 MPa and 8.1 ± 0.8% elongation was
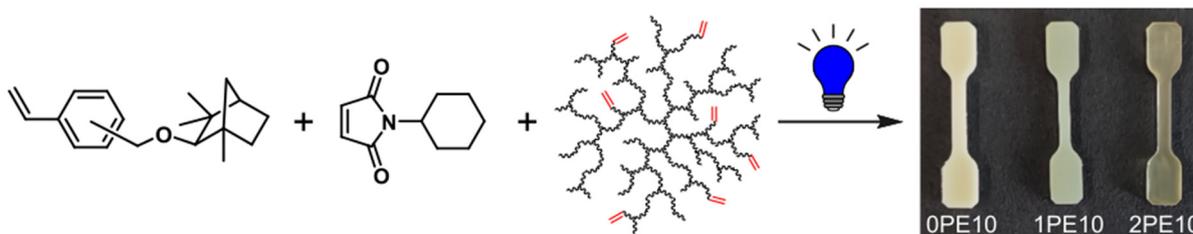
Scheme 2 Selected non-volatile maleimide and styrene derivatives (left) and photocuring into phase separation-exhibiting samples with 10 wt% of **0PE**, **1PE**, and **2PE** (right).
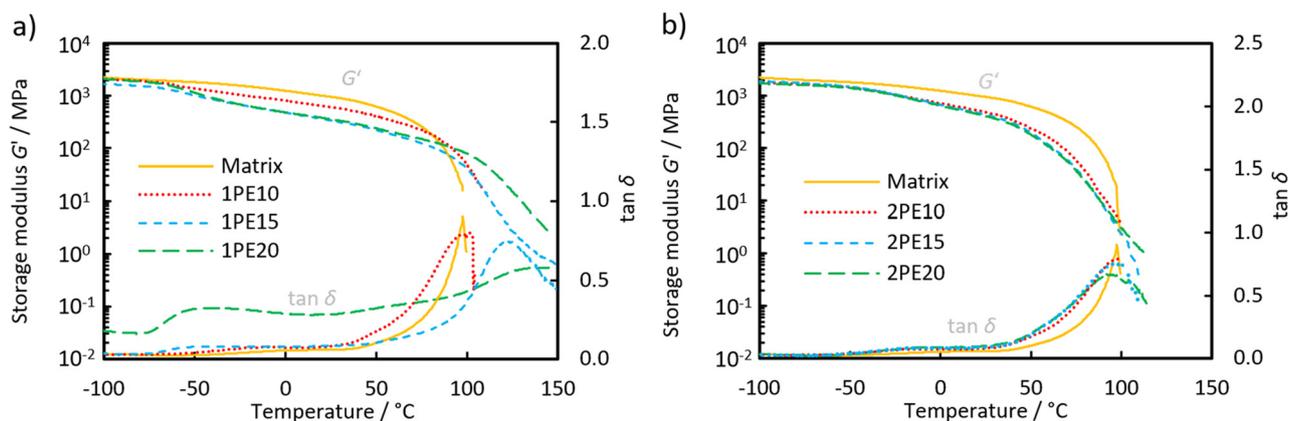
Fig. 1 Storage modulus (G′) and loss factor (tan δ) obtained for (a) **1PE** and (b) **2PE** at various loadings (10, 15, 20 wt%) in the maleimide–styrene matrix compared to the pure matrix in dynamic mechanical thermal analysis.

Table 3 Prepared formulations and their tensile properties: Young's modulus (E), stress (σ) and strain at break (ε), yield stress (σ_Y) and strain at the yield point (ε_Y), and tensile toughness (r)

Formulation	Rubber	E/MPa	σ/MPa	ε/%	σ_Y/MPa	ε_Y/%	r/MJ m^{-3}
Matrix	—	1009 ± 49	5.5 ± 1.0	0.6 ± 0.1	—[b]	—[b]	0.02 ± 0.01
0PE10	10 wt% **0PE**	—[a]	—[a]	—[a]	—[a]	—[a]	—[a]
1PE10	10 wt% **1PE**	699 ± 31	13.0 ± 2.5	2.3 ± 0.6	—[b]	—[b]	0.17 ± 0.07
1PE15	15 wt% **1PE**	398 ± 18	8.5 ± 1.0	2.9 ± 0.4	—[b]	—[b]	0.10 ± 0.08
1PE20	20 wt% **1PE**	332 ± 20	13.1 ± 0.5	51.3 ± 7.1	—[b]	—[b]	5.8 ± 1.0
2PE10	10 wt% **2PE**	534 ± 52	10.6 ± 2.3	2.9 ± 0.3	—[b]	—[b]	0.18 ± 0.04
2PE15	15 wt% **2PE**	477 ± 22	10.6 ± 1.1	3.3 ± 0.5	—[b]	—[b]	0.21 ± 0.05
2PE20	20 wt% **2PE**	355 ± 27	11.1 ± 0.6	56.4 ± 9.9	12.3 ± 0.7	8.1 ± 0.8	6.1 ± 1.3
EPE10	10 wt% **EPE**	—[a]	—[a]	—[a]	—[a]	—[a]	—[a]

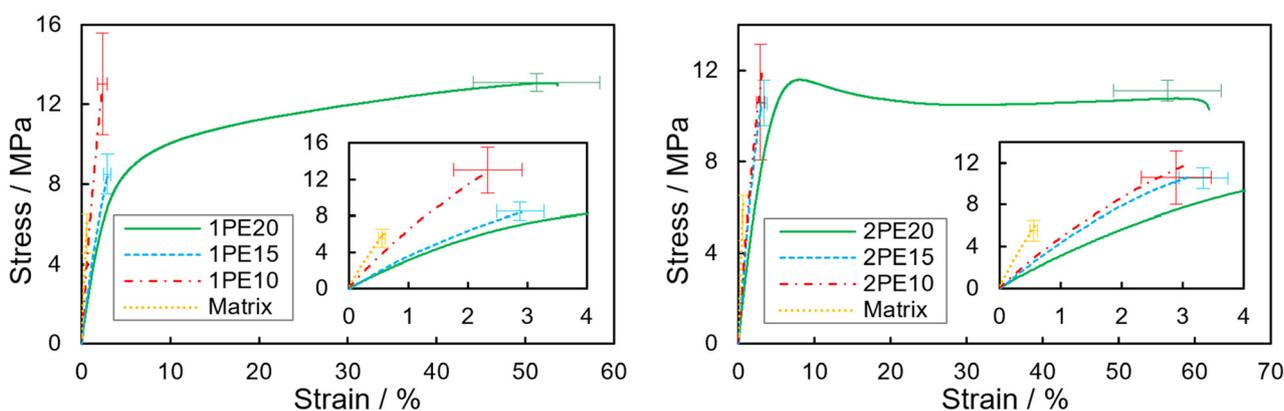[a] Too brittle for testing. [b] No well-defined yielding observed.

Fig. 2 Stress–strain curves of the cured formulations varying in loadings (10, 15, 20 wt%) of (a) **1PE** and (b) **2PE** hyperbranched rubber.

achieved, followed by strain hardening and necking until an ultimate tensile strength of 11.1 ± 0.6 MPa at 56.4 ± 9.9% elongation at break was reached. Both formulations **1PE20** and **2PE20** exhibited significantly enhanced tensile toughness of 5.8 ± 1.0 MJ m^{-3} and 6.1 ± 1.3 MJ m^{-3} respectively, far exceeding the value 0.02 ± 0.01 MJ m^{-3} measured for the matrix.

Material morphology

To explain the unexpected brittle-ductile transition in tensile tests, the prepared materials were analysed *via* scanning electron microscopy (SEM) and atomic force microscopy (AFM). The SEM images of cross-sections from **1PE15** and **2PE15** tensile specimens
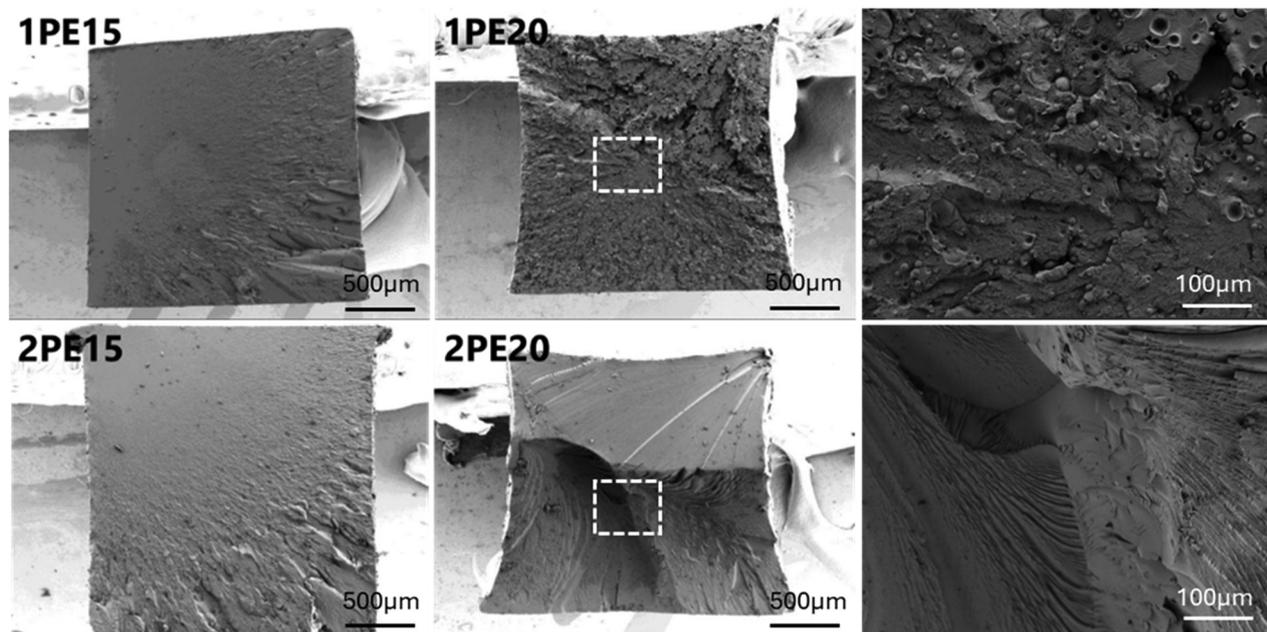
© 2025 The Author(s). Published by the Royal Society of Chemistry

RSC Appl. Polym., 2025, **3**, 1165–1176 | **1169**

Fig. 3 SEM images of fracture surfaces of tensile test specimens: **1PE15**, **1PE20**, **2PE15** and **2PE20**. Larger representations of the images are available in the SI.

reveal brittle fracture surfaces with a rectangular shape (Fig. 3). In contrast to this, samples **1PE20** and **2PE20**, which exhibited high elongation at break during tensile testing, show clear signs of plastic deformation from their original rectangular shape.

The fracture surfaces of **1PE20** and **2PE20** show well-defined heterogeneous morphology with rubber-rich domains embedded in the matrix. These domains (Fig. 3 and 4) contribute to toughening by promoting energy dissipating mechanisms.[42] Evidences of trans-particle fracture indicate strong interfacial adhesion between the rubbers and the matrix, enabling effective stress transfer across the rubber particles (Fig. S7). Moreover, the cleavage planes indicate the tendency
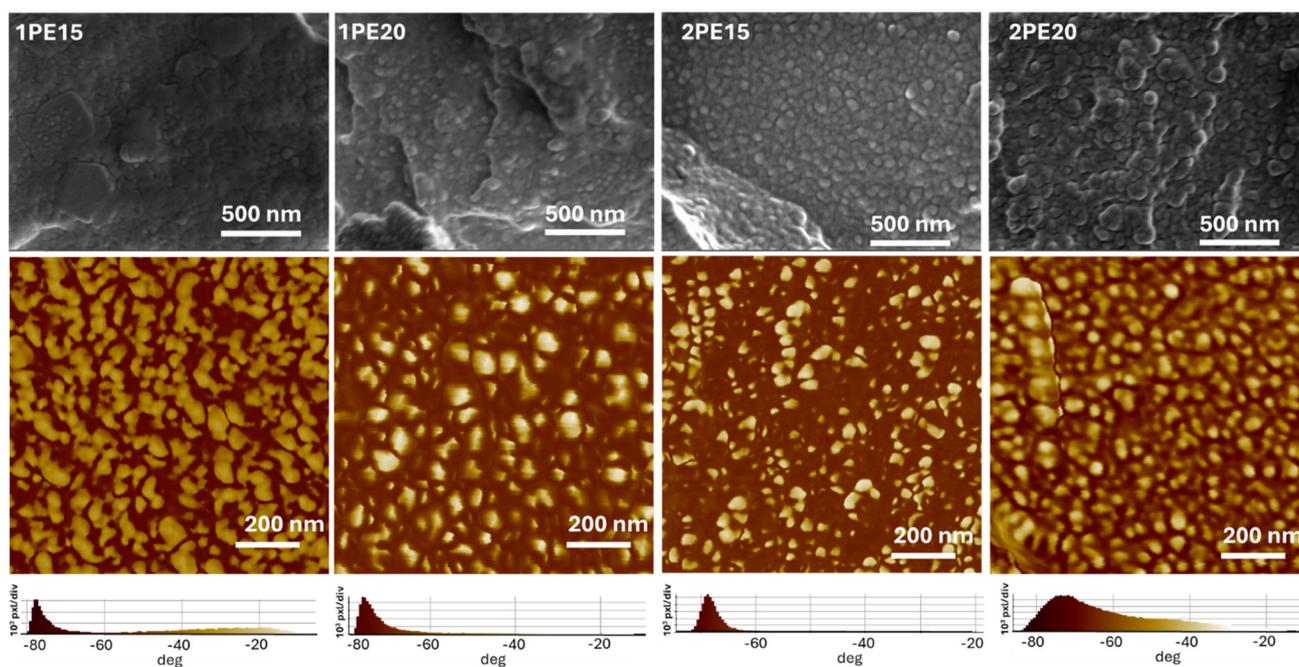

Fig. 4 SEM (top) and AFM (bottom) images of **1PE15**, **1PE20**, **2PE15** and **2PE20** morphologies. Larger representations of the images are available in the SI.

of the matrix towards brittle fracture. Yet crack path deflection by particles, cavitations, and interfacial debonding contribute to increasing fracture toughness by increasing the effective fracture surface area.

Overall, necking and large-scale yielding take place in **1PE20** and **2PE20**, leading to substantially increased values for elongation at break in comparison to the 15 wt% samples. Further microscopic investigation of the morphology of the examined materials using scanning electron microscopy (SEM) and atomic force microscopy (AFM) revealed sub-50 nm domains in all material types (Fig. 4), suggesting that a nanostructured morphology influences the mechanical properties of the materials. This structural arrangement in combination with a varying composition likely plays a role in the observed differences in fracture behaviour between the 15 wt% and 20 wt% samples. The fracture strength of the 15 wt% samples is lower than their elastic limit, resulting in brittle fracture. This can be explained by the lower rubber content in the 15 wt% samples, which leads to a lower fracture toughness. At the same time the elastic limit is higher. Under load, the sample will therefore fracture in a brittle manner before the elastic limit is reached.

Increasing the rubber loading to 20 wt% decreases the mechanical stress at which plastic deformation kicks in. Due to this, the 20 wt% samples reach the elastic limit and start yielding before the fracture strength is reached, leading to macroscopic plastic deformation of the samples as indicated in Fig. 3.

Comparing **1PE20** and **2PE20**, the lower molecular weight and higher functional endgroup content seem to favour yielding behaviour in **2PE20** compared to **1PE20**. The larger **1PE** rubber significantly lowers the initial stress response of the material, resembling the typical behaviour of materials where rubbers are added as additives.

Resin crosslinking behaviour

For an optimal 3D printing process with highest possible resolution and optimized printing speed, kinetic characterization of the thermomechanically best-performing formulation **2PE20** for various curing parameters is required: sufficient light intensity for as fast as possible printing should be chosen, while at the same time the irradiation intensity should be limited to the required dose to avoid overpolymerization and maintain formulation stability over extended time periods. While kinetic studies typically also include a temperature

screening, in this case, the miscibility and viscosity (SI) of the resin mandated the printing temperature to be 80 °C.

For the resin curing experiments, an LED light source was used with light intensities of 10, 20 or 40 mW cm^{-2} at the sample surface. The maximum emmission of the light source at 385 nm matches wavelength of the 3D printer DLP light engine. In a photo-DSC investigation, where the evolving heat of polymerization (ΔH_{pol}) is analysed as a measure for reactivity, similar polymerization onset times were found for all used intensities (1.0–1.3 s, Table 4 and Fig. 5). As expected, an increase in light intensity (10 mW cm^{-2} to 20 mW cm^{-2}) leads to lower times until maximum polymerization heat (t_{max}) is reached (11.2 to 6.9 s). Further increasing the light intensity to 40 mW cm^{-2} changed the t_{max} only slightly, from 6.9 to 6.4 s. The only significant improvement with increasing intensity was observed in the required time to reach 95% of the maximum double bond conversion (t_{95}, from 59.4 to 31.7 s). This parameter is, however, not important for the 3D printing process, as the conversion is usually finetuned for fast resin solidification. Full conversions beyond this point can typically be achieved during the post-processing procedures. Additionally, the measured polymerization heat was lowest in the sample cured at 40 mW cm^{-2}, indicating a possibly reduced network crosslinking quality due to rapid gelation.
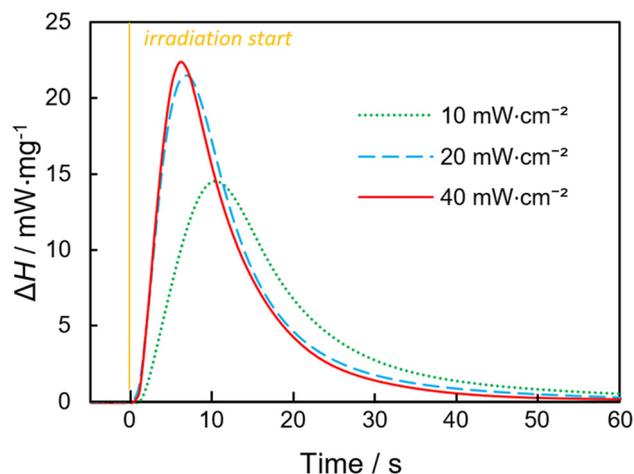

Fig. 5 Photo-DSC curves of **2PE20** formulation curing with an LED (385 nm emission maximum) with intensities of 10, 20 or 40 mW cm^{-2}.

Table 4 Summary of photo-DSC and photorheology data: data obtained for the **2PE20** resin formulation: polymerization heat (ΔH_{pol}); polymerization onset time (t_{ons}); time at which polymerization peak maximum is reached (t_{max}); time at which 95% of final conversion is reached (t_{95}); time until gelation occurs (t_g); double bond conversion at gel point (DBC$_{gel}$); shrinkage force (F_s)

Light intensity mW cm^{-2} [a]	Photo-DSC			Photorheology			
	ΔH_{pol}/J g^{-1}	t_{ons}/s	t_{max}/s	t_{95}/s	t_{gel}/s	DBC$_{gel}$/%	F_s/N
10	279	1.3	11.2	59.4	8.4	33	13.3
20	295	1.0	6.9	42.8	5.4	31	13.2
40	267	1.1	6.4	31.7	4.2	30	11.7

[a] Determined at the sample surface (LED light source with its maximum emission at 385 nm).

The **2PE20** formulation was further analysed using RT-NIR-photorheology under the same light intensity settings (Fig. 6 and Table 4). In accordance with photo-DSC findings, curing at 20 and 40 mW cm^{-2} proceeded with similar curing rates, reaching gel points at 5.4 s and 4.2 s, respectively, at conversions of about 30%. The polymerization at 10 mW cm^{-2} was significantly slower, with the gel point reached at 8.4 s, at 33% double bond conversion, which is in line with the photo-DSC results. The final double bond conversion was found to vary between 95 and 99.9% conversion directly after photocuring. The variation was attributed to the enlarged uncertainty of the integrals of very small areas under the curve found at such high conversions. During curing at 10 and 20 mW cm^{-2}, the maximum shrinkage force reached 13.3 N. Interestingly, in the experiment conducted at 40 mW cm^{-2} light intesity, the recorded shrinkage force was only 11.7 N, further hinting at reduced network crosslinking quality caused by rapid gelation, as also proposed previously based on the photo-DSC results.

As 3D printing is generally performed to the solidification point, with printed objects undergoing post-curing afterward, 20 mW cm^{-2} light intensity was chosen as it provided optimal curing performance in the initial polymerization phase in photo-DSC and photorheology. No significant differences in polymerization behaviour up to the gel point were found between the irradiation intensities of 10 and 20 mW cm^{-2}, suggesting similar phase separation behaviour.

While the intensity of 40 mW cm^{-2} accelerated late-stage curing, it did not improve the initial polymerization rate compared to 20 mW cm^{-2}, likely due to photoinitiator saturation. Such a higher irradiation intensity further increases the likelihood of overpolymerization and thus loss of resolution and increased network inhomogeneities due to rapid gelation at higher irradiation intensities.

Hot lithography

The thermomechanically best-performing formulation **2PE20** was chosen for hot lithography printing at 80 °C using a DLP light engine which matches the 385 nm maximum emission of the previously used LED light source. Due to the supposed inhomogeneities of polymer networks cured at 40 mW cm^{-2} and the significantly lower curing rate at 10 mW cm^{-2}, 20 mW cm^{-2} was selected as optimal irradiation intensity. Subsequently, the 3D printing curing time was optimized in exposure studies. Finally, 3D printing of two complex pyramids demonstrate good material printability (Fig. 7).

The printed pyramids exhibit a well-defined shape, with SEM images showing high precision in details such as the detailed pyramid corners and strong interlayer connectivity.

Materials and methods

The chemicals vinylbenzyl chloride (mixture of *meta* and *para* substituted isomers, Sigma-Aldrich), sodium hydride (TCI Chemicals), fenchol (Sigma-Aldrich), *N*-cyclohexyl maleimide (Angene chemical), ammonium chloride (Carl Roth), anhydrous sodium sulphate (VWR), 4-methoxyphenol (Sigma-Aldrich), triethylamine (Sigma-Aldrich), and 10-undecenoic acid (Alfa Aesar) were purchased from their respective suppliers and used without any further purifications. Commercial grade solvents dry dimethylformamide (Sigma Aldrich), diethyl ether (Donau Chemie), *n*-hexane (Donau Chemie) and petroleum ether (Donau Chemie) were used as purchased. Commercial grade dichloromethane (DCM, Donau Chemie) was dried using a PureSolv system (Inert), stored over 3 Å molecular sieves and stripped with argon for 15 min prior to polymerization with **Pd**. The photoinitiator ethyl (2,4,6-trimethylbenzoyl) phenyl (Speedcure TPO-L) was kindly gifted by Lambson. Fenchyl styrene was prepared using the procedure described in literature.[21] Palladium α-diimine catalyst **Pd** was synthesized as described in literature.[28]

NMR spectra were measured on a Bruker Avance DRX-400 FT-NMR spectrometer (400 MHz for ^{1}H- and 101 MHz for ^{13}C-NMR) in CDCl$_3$ at room temperature. Relaxation time was increased to 10 s for polymer samples. Chemical shifts were referenced to the residual solvent peak of CDCl$_3$ (7.26 ppm for
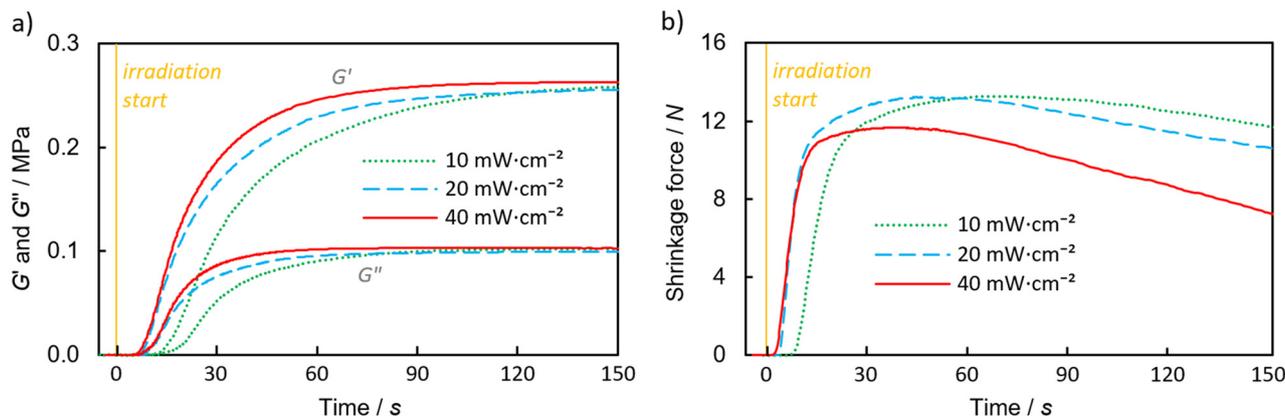

Fig. 6 RT–NIR-photorheology curves of **2PE20** formulation curing at varying intensities with an LED (maximum emission centered around 385 nm): (a) storage (*G'*) and loss modulus (*G''*) and (b) shrinkage force development with curing time.
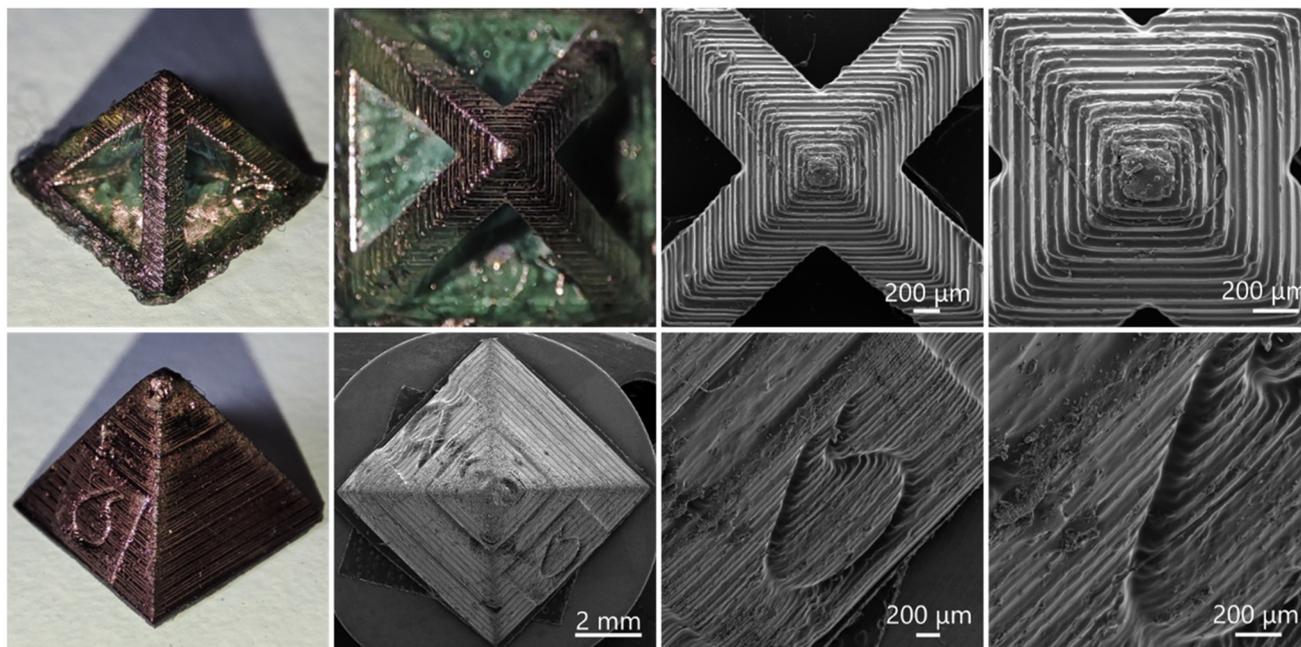
Fig. 7 Two Au nanocoated 3D printed pyramids and their zoomed SEM images.

^{1}H, 77.16 ppm for ^{13}C). All recorded spectra are included in the SI. The molar mass of the prepared polymers was characterized by size-exclusion chromatography using a Waters Breeze chromatograph (solvent pump Waters 1515, autosampler Waters 717+, refractometric detector Waters 2410 and a multi-angle light scattering detector miniDawn TREOS (Wyatt) at angles 45°, 90° and 135°). Separation was performed on two columns PSS Lux LIN M 5 μm (7.8 × 300 mm) at 35 °C and mobile phase flow of 1 mL min^{-1} (THF). Injection volume was 100 μL of sample solution in tetrahydrofuran at a concentration of approximately 3 mg mL^{-1}. HR-MS spectrum was measured from HPLC-grade acetonitrile solution (10 μM) using an Agilent 6230 AJS ESITOF mass spectrometer (Agilent Technologies) equipped with HTC PAL system autosampler (CTC Analytics AG), separated by an Agilent 1100/1200 HPLC with binary pumps, degasser, and column thermostat (Agilent Technologies).

Experimental

Synthesis of 2-(methacryloyloxy)ethyl undec-10-enoate (MEU)

10-Undecenoic acid (18.4 g, 100 mmol) was dissolved in 50 mL of dichloromethane (DCM) in a round bottom flask under inert conditions and the reaction mixture was cooled down to 0 °C. A drop of dimethyl formamide was added and oxalyl chloride (14 g, 110 mmol) was added dropwise thereafter. After two hours of stirring at 0 °C, the flask was left to warm up to room temperature. DCM and the unreacted oxalyl chloride were removed under vacuum. 50 mL dry DCM were then added and the reaction mixture was cooled to 0 °C. 2-Hydroxyethyl methacrylate (13.4 g, 100 mmol) and triethyl-

amine (11.2 g, 110 mmol) were added slowly and the reaction mixture was left to react for two more hours. The reaction mixture was then diluted with 200 mL diethyl ether and extracted three times with 200 mL water to remove any impurities. The organic phase was further extracted with 200 mL brine and dried over anhydrous magnesium sulphate. The solvents were removed under vacuum and silica column chromatography using hexane as a mobile phase was run to purify the product, yielding 24.9 g of colourless liquid (84%) after drying under vacuum.

^{1}**H-NMR** (400 MHz, CDCl$_3$) δ: 6.13–6.10 (m, 1H, =C**H**–C), 5.86–5.75 (m, 1H, =C**H**–CH$_2$), 5.59 (p, J = 1.6 Hz, 1H, =C**H**–C), 5.08–4.89 (m, 2H, =C**H**–C), 4.40–4.26 (m, 4H, O–C$_2$H$_4$–O), 2.32 (t, J = 7.5 Hz, 2H, –C**H$_2$**–COO), 2.03 (q, J = 6.6 Hz, 2H, =CH–C**H$_2$**–), 1.96–1.93 (m, 3H, C**H$_3$**–C), 1.62 (p, J = 7.3 Hz, 2H, –C**H$_2$**–CH$_2$–CO$_2$), 1.41–1.24 (m, 10H). ^{13}**C-NMR** (101 MHz, CDCl$_3$) δ: 173.72 (CH2–**C**OO), 167.25 (C–**C**OO), 139.22 (=**C**H–), 136.10 (**C**=CH2), 126.14 (C=**C**H2), 114.29 (**C**H$_2$=CH–), 62.61 (–O–**C**H$_2$–), 62.01 (–O–**C**H$_2$–), 34.28, 33.92, 29.41, 29.34, 29.20, 29.03, 25.03, 18.41. **HR-MS** (ACN, ESI+, m/z): calcd: 297.2061 [M + H]$^+$; found: 297.2061 [M + H]$^+$.

Copolymerization of ethene and MEU

A Fisher-Porter vessel equipped with magnetic stir bar was evacuated and filled with ethene. After heating up to 35 °C, dry and argon-stripped DCM and monomer were added under nitrogen counterflow. The vessel was pressurized with ethene for 15 min to saturate the reaction mixture. The polymerization reaction was started through addition of 10 μmol **Pd** catalyst in 1 mL DCM. After 24 h, the reaction mixture was poured into methanol. The precipitated polymer was then dissolved in

DCM and the precipitation step was repeated two more times in order to remove any residual impurities. After drying under vacuum, the product was stabilized with 100 ppm of 4-methoxyphenol (MeHQ) and stored at 4 °C.

Formulation preparation

Formulations were prepared in 3–6 g batches using the following procedure: the hyperbranched polyethylene rubber (10, 15 or 20 wt%) was dissolved in DCM for easy transfer to a round bottom flask. The photoinitiator ethyl phenyl(2,4,6-trimethylbenzoyl)phosphinate (TPO-L, 1 wt%), and the monomers N-cyclohexyl maleimide and fenchyl styrene were added and upon homogenization, the solvent was removed and the formulation was degassed under reduced pressure at 80 °C. The mixture was kept at 80 °C until photo-DSC, photorheology or hot lithography was performed.

Bulk curing

Specimens for DMTA and tensile testing were prepared by formulation curing in silicone moulds at 80 °C using a UVET LED light source with emission maximum at 365 nm and 290 mW cm^{-2} light intensity at the sample surface. The samples were irradiated for 180 s, removed from silicone moulds, rotated upside down and irradiated for additional 180 s. No additional post-curing steps were undertaken.

Analytical methods

Tensile testing. Five dumbbell specimens (ISO 527 shape 5B) per material were tested on a Zwick Z050. The crosshead speed was 5 mm min^{-1}. The stress–strain plot was recorded and characteristic mean values at the yield point and at break were extracted from the resulting curves for five separate samples.

Dynamic mechanical thermal analysis. The temperature sweep was performed on an Anton Paar MCR 301 with a CTD 450 oven and an SRF 12 measuring system in torsion mode with a frequency of 1 Hz, strain of 0.1%, constant normal force of −1 N and a temperature ramp of 2 °C min^{-1} from −100 to 250 °C. Data were recorded with the software Rheoplus/32V3.40 from Anton Paar.

Scanning electron microscopy. The 3D printed pyramids were imaged on a Tescan Vega 3 LMU at 15 kV acceleration voltage. The surfaces of samples were coated with approximately 10 nm gold prior to imaging to make them conductive. Fracture surface images of the samples were taken with a Tescan Clara FEG-SEM at 1 kV acceleration voltage. The samples were sputter-coated with gold under argon atmosphere.

Atomic force microscopy. Microstructure characterization was further performed using an XE7-Park Systems Atomic Force Microscopy in tapping mode, and the resulting data were analysed with the built-in XEI data processing tool. The fracture surfaces were obtained by cryo-fracturing in liquid nitrogen, and when smoother surfaces were required, cryo-ultramicrotomy was performed. The surfaces were scanned over an area of 1 × 1 μm^2, with a scan resolution of 256 × 256 pixels and a scan rate ranging from 0.3 to 0.7 Hz. The AFM cantilever used (AC160TS Olympus) had a tetrahedral silicon tip with an approximate radius of 7 nm, a spring constant of 26 N m^{-1}, and a free oscillation frequency near 300 kHz.

Photo-DSC. Photo-differential scanning calorimetry (photo-DSC) experiments were performed at 100 °C in triplicates on a Netzsch DSC 204 F1 equipped with an autosampler under nitrogen inert atmosphere. An LED light source (maximum emission at 385 nm UV light, matching the wavelength of the used DLP printer) was calibrated with respect to intensity at the sample surface using an Ocean Optics USB 2000+ spectrometer and used for the measurements. The samples were irradiated twice for 300 s. The second irradiation cycle was performed for correction of heat effects from the curing light. The difference in heat flow was recorded as a function of time and evaluated using Netzsch Proteus software. Polymerization onset time (t_{onset}) and time at which polymerization peak maximum is reached (t_{max}) were evaluated from the heat flow curve. Polymerization heat (ΔH_{pol}) was calculated by integrating the area under the heat flow curve; the time to reach 95% of the final conversion (t_{95}) was estimated as the point at which the polymerization heat achieves 95% of the total polymerization heat value.

RT-NIR-photorheology. Photorheology data were obtained using an Anton Paar MCR 302 WESP rheometer equipped with a P-PTD 200/GL Peltier Glass Plate and a plate-plate PP25 measuring system. An LED light source (maximum emission at 385 nm, matching the wavelength of the used DLP printer) was calibrated with respect to intensity at the sample surface using an Ocean Optics USB 2000+ spectrometer and used for the measurements. Each experiment was performed with 150 μL of the formulation at 100 °C with a constant gap size of 200 μm, shear strain of 1% and frequency of 1 Hz. The storage modulus (G') and loss modulus (G'') were recorded every 0.2 s during the irradiation using the software Rheoplus/32V3.40 from Anton Paar. The approximate gel point of a formulation was estimated from the storage modulus (G') and loss modulus (G'') crossover point. The curing process was monitored in situ by recording time-resolved NIR spectra in 0.25 s intervals using the software OPUS 7.0. The double bond conversion (DBC) was calculated as a ratio of the relevant peak area (6080–6250 cm^{-1}) in given time (A_c) divided by the peak area prior to irradiation (A_u) (1).

$$\text{DBC} = \frac{A_c}{A_u} \qquad (1)$$

Hot lithography. Hot lithography was performed on a custom printer using a 385 nm DLP light engine. The printing parameters were as follows: 80 °C heated vat temperature, 80 °C build plate temperature, 50 μm layer height, 20 mW cm^{-2} light intensity at the sample surface for regular layers and 25 mW cm^{-2} for the first layer, exposure time 8 s for regular layers and 12 s for the first layer, lift height 6 mm, peeling speed 25 mm min^{-1}, lift speed 500 mm min^{-1}.

Conclusions

In this work, we have developed a new route for *in situ* functionalization of hyperbranched polyethylene rubber with methacrylate groups by direct copolymerization of ethene with a tailored comonomer and functional-group tolerant metal catalyst. The prepared methacrylated elastomers were used for toughening of a photopolymer matrix based on substituted maleimide and styrene monomers. All tested materials exhibit strains at break, which improved by a factor of 10^3 compared to the pure matrix or the matrix toughened with a comparable non-reactive hyperbranched rubber macromonomer, while exhibiting only minor softening and maintaining their high onsets of T_gs. The best sample **2PE20** exhibited a yield point and necking typically observed in non-crosslinked thermoplastic materials during tensile testing while maintaining a high glass transition temperature. This formulation was further investigated using photo-DSC and RT-NIR-photorheology to discover optimal curing parameters for hot lithography using a 385 nm DLP light engine. Finally, the optimized exposure parameters were used to demonstrate printability. Both prints exhibit high levels of detail and good interlayer adhesion demonstrating the good printability of this toughened material.

Author contributions

Vojtěch Musil: conceptualization, investigation, methodology, validation, formal analysis, data curation, writing – original draft, writing – review & editing, visualization; Dominik Laa: investigation (3D printing), formal analysis; Mojtaba Ahmadi: investigation (morphology chapter), formal analysis; Jürgen Stampfl: funding acquisition, formal analysis, writing – review & editing; Robert Liska: funding acquisition, formal analysis, writing – review & editing; Jan Merna: funding acquisition, writing – review & editing; Katharina Ehrmann: supervision, conceptualization, methodology, formal analysis, writing – original draft, writing – review & editing.

Conflicts of interest

There are no conflicts to declare.

Data availability

Data for this article, including NMRs, SECs photo-DSC, photorheology, tensile testing, DMTA and AFM data, are available at TU Wien Research Data at **https://doi.org/10.48436/hzgm2-h1q44**.

Supplementary information is available. See DOI: **https://doi.org/10.1039/d5lp00138b**.

Acknowledgements

References

1 S. F. Iftekar, A. Aabid, A. Amir and M. Baig, *Polymers*, 2023, **15**, 2519.
2 K. Deshmukh, M. T. Houkan, M. A. AlMaadeed and K. K. Sadasivuni, *3d and 4d Printing of Polymer Nanocomposite Materials: Processes, Applications, and Challenges*, 2020, pp. 1–24, DOI: **10.1016/B978-0-12-816805-9.00001-6**.
3 B. Berman, *Bus. Horiz.*, 2012, **55**, 155–162.
4 M. Lee, R. Rizzo, F. Surman and M. Zenobi-Wong, *Chem. Rev.*, 2020, **120**, 10670–10747.
5 N. Hossain, M. A. Chowdhury, M. B. A. Shuvho, M. A. Kashem and M. Kchaou, *J. Mater. Eng. Perform.*, 2021, **30**, 4756–4767.
6 A. Afridi, A. Al Rashid and M. Koç, *Bioprinting*, 2024, **43**, e00360.
7 R. Song and C. Telenko, Material Waste of Commercial FDM Printers under Realstic Conditions, In Solid Freeform Fabrication 2016: Proceedings of the 26th Annual International Solid Freeform Fabrication Symposium – An Additive Manufacturing Conference, 2016.
8 C. Mendes-Felipe, J. Oliveira, I. Etxebarria, J. L. Vilas-Vilela and S. Lanceros-Mendez, *Adv. Mater. Technol.*, 2019, **4**, 1800618.
9 S. C. Ligon-Auer, M. Schwentenwein, C. Gorsche, J. Stampfl and R. Liska, *Polym. Chem.*, 2016, **7**, 257–286.
10 C. Decker, T. N. T. Viet, D. Decker and E. Weber-Koehl, *Polymer*, 2001, **42**, 5531–5541.
11 P. Esfandiari, S. C. Ligon, J. J. Lagref, R. Frantz, Z. Cherkaoui and R. Liska, *J. Polym. Sci., Part A: Polym. Chem.*, 2013, **51**, 4261–4266.
12 R. Bagheri, B. T. Marouf and R. A. Pearson, *Polym. Rev.*, 2009, **49**, 201–225.
13 C. Grein and M. Gahleitner, *eXPRESS Polym. Lett.*, 2008, **2**, 392–397.
14 J. Rovere, C. A. Correa, V. G. Grassi and M. F. Dal Pizzol, *J. Mater. Sci.*, 2008, **43**, 952–959.
15 S. Guessasma, S. Belhabib and H. Nouri, *Macromol. Mater. Eng.*, 2019, **304**, 1800793.
16 K. Gong, H. D. Liu, C. Huang, Z. Cao, E. Fuenmayor and I. Major, *Polymers*, 2022, **14**, 5093.
17 M. Arif, D. Kumar and A. N. Siddiquee, *J. Mater. Eng. Perform.*, 2024, **33**, 6769–6779.
18 R. J. A. Roncallo, L. L. L. Taborda and D. Guillen, *Rapid Protot. J.*, 2024, **30**, 145–160.
19 C. Kasprzak, J. R. Brown, K. Feller, P. J. Scott, V. Meenakshisundaram, C. Williams and T. Long, *ACS Appl. Mater. Interfaces*, 2022, **14**, 18965–18973.
20 P. J. Scott, V. Meenakshisundaram, M. Hegde, C. R. Kasprzak, C. R. Winkler, K. D. Feller, C. B. Williams

© 2025 The Author(s). Published by the Royal Society of Chemistry

RSC Appl. Polym., 2025, **3**, 1165–1176 | **1175**

and T. E. Long, *ACS Appl. Mater. Interfaces*, 2020, **12**, 10918–10928.

21 J. Steindl, K. Ehrmann, C. Gorsche, C. C. Huang, T. Koch, P. Steinbauer, A. Rohatschek, O. G. Andriotis, P. J. Thurner, A. Prado-Roller, J. Stampfl and R. Liska, *Polym. Int.*, 2022, **71**, 856–866.

22 M. Imanaka, I. Narita, Y. Nakamura, S. Hisaka, K. Fujiwara, S. Yoshida and K. Hara, *J. Mater. Sci.*, 2021, **56**, 1842–1854.

23 K. Zhao, X. X. Song, C. S. Liang, J. Wang and S. A. Xu, *Iran. Polym. J.*, 2015, **24**, 425–435.

24 S. R. Mousavi, S. Estaji, M. R. Javidi, A. Paydayesh, H. A. Khonakdar, M. Arjmand, E. Rostami and S. H. Jafari, *J. Mater. Sci.*, 2021, **56**, 18345–18367.

25 W. Tessanan, P. Daniel and P. Phinyocheep, *Polymers*, 2023, **15**, 4287.

26 D. Mondal, Z. Haghpanah, C. J. Huxman, S. Tanter, D. Sun, M. Gorbet and T. L. Willett, *Mater. Sci. Eng., C*, 2021, **130**, 112456.

27 Y. S. Chen, L. Wang, H. J. Yu, Y. L. Zhao, R. L. Sun, G. H. Jing, J. Huang, H. Khalid, N. M. Abbasi and M. Akram, *Prog. Polym. Sci.*, 2015, **45**, 23–43.

28 L. K. Johnson, C. M. Killian and M. Brookhart, *J. Am. Chem. Soc.*, 1995, **117**, 6414–6415.

29 B. K. Long, J. M. Eagan, M. Mulzer and G. W. Coates, *Angew. Chem., Int. Ed.*, 2016, **55**, 7106–7110.

30 I. D'Auria, M. Maggio, G. Guerra and C. Pellecchia, *Macromolecules*, 2017, **50**, 6586–6594.

31 F. He, D. Wang, A. Wu, B. Jiang, Z. Zhang, Z. Cheng, Z. Fu, Q. Zhang and Z. Fan, *Appl. Organomet. Chem.*, 2018, **32**, e4566.

32 Y. Chen, L. Wang, H. Yu, Y. Zhao, R. Sun, G. Jing, J. Huang, H. Khalid, N. M. Abbasi and M. Akram, *Prog. Polym. Sci.*, 2015, **45**, 23–43.

33 G. H. Chen, X. S. Ma and Z. B. Guan, *J. Am. Chem. Soc.*, 2003, **125**, 6697–6704.

34 D. Takeuchi and K. Osakada, *Polymer*, 2016, **82**, 392–405.

35 S. Morgan, Z. Ye, K. Zhang and R. Subramanian, *Macromol. Chem. Phys.*, 2008, **209**, 2232–2240.

36 S. Song, A. Wu, Y. Yu, P. Yang, Z. Fu and Z. Fan, *J. Polym. Sci., Part A:Polym. Chem.*, 2017, **55**, 1900–1909.

37 J. M. Santos, M. R. Ribeiro, M. F. Portela, H. Cramail and A. Deffieux, *Macromol. Chem. Phys.*, 2001, **202**, 3043–3048.

38 J. Wang, K. Zhang and Z. Ye, *Macromolecules*, 2008, **41**, 2290–2293.

39 G. Sun and Z. Guan, *Macromolecules*, 2010, **43**, 4829–4832.

40 S. Mecking, L. K. Johnson, L. Wang and M. Brookhart, *J. Am. Chem. Soc.*, 1998, **120**, 888–899.

41 M. L. Auad, P. M. Frontini, J. Borrajo and M. I. Aranguren, *Polymer*, 2001, **42**, 3723–3730.

42 M. Ahmadi, K. Ehrmann, T. Koch, R. Liska and J. Stampfl, *Chem. Rev.*, 2024, **124**, 3978–4020.